Mixed-dimensional WS$_2$/WSe$_2$/Si unipolar barrier heterostructure for high-performance photodetection

Zihao Huang[1], Mengmeng Yang[1], Zhicong Qiu[1], Zhongtong Luo[1], Yu Chen[2*], Chun Du[3*], Jiandong Yao[4], Huafeng Dong[5], Zhaoqiang Zheng[1*] and Jingbo Li[6]

ABSTRACT The use of unipolar barrier structures that can selectively block dark current but allow photocurrent to flow unimpededly has emerged as an effective strategy for constructing high-performance photodetectors. In particular, two-dimensional (2D) materials with tunable band structures and self-passivated surfaces not only satisfy band-matching requirements but also avoid interface defects and lattice mismatches, which are attractive for designing unipolar barriers. Here, we demonstrate a mixed-dimensional WS$_2$/WSe$_2$/p-Si unipolar barrier photodetector, in which 2D WS$_2$ acts as the photon absorber, atomically thin WSe$_2$ as the unipolar barrier, and 3D p-Si as the photogenerated carrier collector. The intercalated WSe$_2$ not only mitigates detrimental substrate effects but also forms a high-conduction band barrier to filter out several dark current components with the photocurrent flowing unimpededly. Driven by tunneling and carrier multiplication effects, the WS$_2$/WSe$_2$/p-Si device exhibits a high light on/off ratio above 10^5, a high detectivity of 2.39 × 10^{12} Jones, and a fast rise/decay time of 8.47/7.98 ms. These figures of merit are significantly improved over the conventional WS$_2$/p-Si device, opening up an effective scheme for designing high-performance optoelectronic devices.

Keywords: unipolar barrier structure, mixed-dimensional device, WS$_2$/WSe$_2$/p-Si heterojunctions, photodetector, dark current suppression

INTRODUCTION

Due to their distinctive properties, including strong light-matter coupling [1,2], tunable band structure [3–5], self-passivated surface [6,7], and high carrier mobility [8–10], two-dimensional (2D) materials have reignited enthusiasm for designing novel optoelectronic devices. In recent years, various 2D material-based photodetectors have demonstrated unique optoelectronic properties through appropriate material selection and device structure design [11–14]. 2D material-based photodetectors

operated in the photoconductive mode tend to feature high responsivity with high photogain, but these devices suffer from large dark current, low detectivity, and slow response speed [15,16]. Although constructing p-n junctions or p-i-n junctions is an effective scheme to suppress device dark current and improve detectivity, the depletion regions sacrifice device responsivity [7,15]. For popularized applications, photodetectors should simultaneously possess high responsivity, high light on/off ratio, high detectivity, and fast response speed [17]. To satisfy these requirements, photodetectors with unipolar barrier structures provide an innovative avenue through carefully engineering band structures [18,19]. To date, numerous unipolar barrier photodetectors have been successfully assembled through epitaxial growth or layer stacking techniques [20]. For example, infrared photodetectors employing all-3D III–V and HgCdTe materials have demonstrated advanced photodetection capabilities [18,21,22]. In addition, unipolar barrier photodetectors based on all-2D WS$_2$/h-BN/PdSe$_2$ achieve a high light on/off ratio of 10^6 and detectivity of 2.7 × 10^{12} Jones [7]. Despite the considerable progress, few attempts have been made to construct 2D/3D mixed-dimensional unipolar barrier photodetectors. In fact, a 2D/3D mixed-dimensional structure offers an opportunity to combine their respective advantages to explore fundamental carrier transport phenomena and exploit them in devices [23–27]. 3D Si technology is very mature, and it is easy to transfer 2D materials onto 3D Si substrates. The combination of 2D materials with 3D semiconductors has paved the way for the future large-scale production of high-performance optoelectronic devices compatible with mainstream semiconductor processes. In addition, the layer-dependent tunable band structures of different 2D materials can meet the stringent requirements for band alignment in unipolar barrier heterostructures. Moreover, conventional unipolar barrier photodetectors are based on nBn or pBp structures (n- or p-type photon absorber, barrier layer, and n- or p-type photogenerated carrier collector) [7,19,22,28], where photogenerated carriers are easy to recombine with the majority carriers in the collectors.

[1] Guangdong Provincial Key Laboratory of Information Photonics Technology, School of Materials and Energy, Guangdong University of Technology, Guangzhou 510006, China
[2] Analysis and Test Center, Guangdong University of Technology, Guangzhou 510006, China
[3] Guangdong Provincial Key Laboratory of Optical Fiber Sensing and Communications, Institute of Photonics Technology, Jinan University, Guangzhou 511443, China
[4] State Key Laboratory of Optoelectronic Materials and Technologies, Nanotechnology Research Center, School of Materials Science & Engineering, Sun Yat-sen University, Guangzhou 510275, China
[5] School of Physics and Optoelectronic Engineering, Guangdong University of Technology, Guangzhou 510006, China
[6] Institute of Semiconductors, South China Normal University, Guangzhou 510631, China
* Corresponding authors (emails: atc_chenyu@gdut.edu.cn (Chen Y); duchun@jnu.edu.cn (Du C); zhengzhq5@mail2.sysu.edu.cn (Zheng Z))

In this work, a mixed-dimensional $WS_2/WSe_2/p-Si$ unipolar barrier photodetector was demonstrated, in which 2D multilayer WS_2 was used as the photon absorber, atomically thin WSe_2 as the unipolar barrier for electrons, and 3D p-Si as the photogenerated carrier collector. The detector has an nBp structure, and the rational barrier arrangement allows the efficient transfer of photogenerated holes in 2D $n-WS_2$ to 3D p-Si while blocking several dark current components. Driven by tunneling and carrier multiplication effects, the $WS_2/WSe_2/p-Si$ device presents outstanding photodetection capabilities, including a light on/off ratio above 10^5, responsivity of 3.72 A W^{-1}, detectivity of 2.39×10^{12} Jones, and rise/decay time of 8.47/7.98 ms. These values are far superior to their counterparts in conventional WS_2/Si devices, depicting a unique landscape of revolutionary advancement in mixed-dimensional optoelectronic devices.

EXPERIMENTAL SECTION

Preparation of WSe_2 flake
WSe_2 nanoflakes with a large size and high quality were prepared in a tube furnace through a modified physical vapor deposition (PVD) process. High-purity WSe_2 powder (99.99%, Aladdin) was used as the growth source and placed in the central region of the heating zone. Then, clean SiO_2/Si (300 nm/500 μm) substrates were placed on the edge of the heating zone. Next, argon gas (99.999%) at a flow rate of 100 standard cubic centimeter per minute (sccm) was introduced into the tube furnace for 20 min to purge the impurities and excess gas, ensuring a clean environment for material growth. Subsequently, the tube furnace was heated to 1100–1150°C. During the heating process, reverse argon gas (pointing from the substrates to the growth source) was introduced at a flow rate of 50 sccm to avoid uncontrolled nucleation. Once heated to the growth temperature, argon gas flowed forward (pointing from the growth source to the substrates) at a flow rate of 110 sccm for 10 min. Finally, the system was naturally cooled to room temperature.

Device fabrication
The $WS_2/WSe_2/Si$ device was fabricated on a $SiO_2/p-Si$ wafer (p-Si resistivity: 1–10 Ω cm^{-2}, p-Si thickness: 500 μm, SiO_2 thickness: 300 nm). First, a photoresist (ARP-5350, Taizhou Sunano New Energy Co., Ltd.) was spin-coated onto the wafer, followed by baking at 100°C for 4 min. Second, a square window (100 μm × 100 μm) was defined by ultraviolet (UV) photolithography (maskless photolithography machine of TuoTuo (Suzhou) Technology Co., Ltd.) in the photoresist. Then, reactive-ion etching (Oxford Estrelas) processes were performed to etch away the SiO_2 layer inside the square window, and the bottom p-Si was exposed. Similarly, several square windows in the $SiO_2/p^{++}-Si$ wafer (p-Si resistivity: < 0.001 Ω cm^{-2}, SiO_2 thickness: 300 nm) were also etched. Third, PVD-grown WSe_2 flakes were transferred onto the edge of square windows with the assistance of poly(methyl methacrylate) [29]. Next, WS_2 flakes with various thicknesses were mechanically exfoliated from bulk WS_2 crystals (Shanghai Onway Technology Co., Ltd.) and transferred onto the WSe_2/Si heterostructures aligned by an optical microscope. Electrical contacts on WS_2 flakes were patterned by UV photolithography. Afterward, Ti/Au (10/60 nm) electrodes were deposited *via* electron beam evaporation. Ag (100 nm) electrodes on the back of Si were fabricated *via* sputtering. Finally, the devices were annealed at 150°C for 1.5 h to remove stresses and impurities from the materials.

Device characterization
The morphology, structure, and composition of the samples were analyzed by a microscope (Motic, BA310MET), a transmission electron microscopy (TEM) system (FEI, Thermo Scientific Talos F200S), and an X-ray photoelectron spectroscopy (XPS) system (Thermo Fisher, Escalab 250Xi). The atomic force microscopy (AFM) and Kelvin probe force microscopy (KPFM) measurements were performed using a scanning probe microscope (Bruker, Dimension FastScan). Raman and photoluminescence (PL) spectra were collected using a confocal microscope (HORIBA Jobin Yvon, LabRAM HR Evolution) with a 532-nm laser excitation. The optoelectronic properties of the prepared devices were characterized using a Keithley 2636b source table with a probe station. The response time was recorded by an oscilloscope (Tektronix, DPO4102B). The incident light source was a 405-nm laser (CNIlaser) and a tungsten bromine lamp (Zolix). The spot diameter was up to 3 mm, which can irradiate the entire photosensitive area (exposed WS_2).

RESULTS
A typical optical microscopic image of the PVD-grown WSe_2 flakes is shown in Fig. 1a, which clearly shows a triangular geometry with a domain size of approximately 120 μm. To further investigate the structural properties and crystal quality of the as-grown WSe_2 flakes, PL, AFM, XPS, and TEM characterizations were performed. As shown in the inset of Fig. 1b, WSe_2 presents conspicuous PL emission with a peak at 755 nm, which can be attributed to the indirect bandgap emission of WSe_2 [30]. Fig. 1b presents the PL intensity mapping at 755 nm. The PL intensity of the whole flake is uniform, indicating the high homogeneity of WSe_2. The AFM morphological image at the edge of the WSe_2 flake shows a thickness of approximately 1.3 nm (Fig. 1c), which indicates its bilayer nature [31]. Then, XPS measurements were performed to investigate the constituent element and binding energy. The survey scan XPS spectrum in Fig. S1a shows the presence of only Se, W, C, and O elements. High-resolution XPS scans of the W 4f and Se 3d signals are presented in Fig. S1b, c, respectively. Deconvolution analysis results reveal that the peaks at 32.8 and 34.9 eV can be ascribed to W^{4+} $4f_{7/2}$ and W^{4+} $4f_{5/2}$, respectively [32]. Moreover, two peaks at 35.3 and 36.1 eV were observed, which are the footprints of W^{6+} $4f_{7/2}$ and W^{6+} $4f_{5/2}$, respectively. The two peaks may originate from the sporadical oxidation reaction of WSe_2 during exposure to air [33,34]. This slight oxide layer has been reported to prolong the lifetime of photogenerated carriers and lead to increased photoresponse [35,36]. Furthermore, the peaks at 54.7 and 55.8 eV can be assigned to Se $3d_{5/2}$ and Se $3d_{3/2}$, respectively, confirming the formation of Se^{2-} [33].

Sequentially, TEM measurements were performed to investigate the microstructure of WSe_2. Fig. 1d shows the low-magnification TEM image of a trigonal WSe_2 flake transferred onto a copper grid. The high-resolution TEM (HRTEM) image in Fig. 1e presents a perfect honeycomb atomic structure, which fits the hexagonal-phase model of WSe_2. The lattice spacing was measured to be 0.279 nm, corresponding to the (-1100), (01-10), and (10-10) planes of WSe_2. The selected-area electron diffraction patterns in Fig. 1f exhibit a single set of sixfold symmetric electron diffraction, confirming its single-crystal feature.
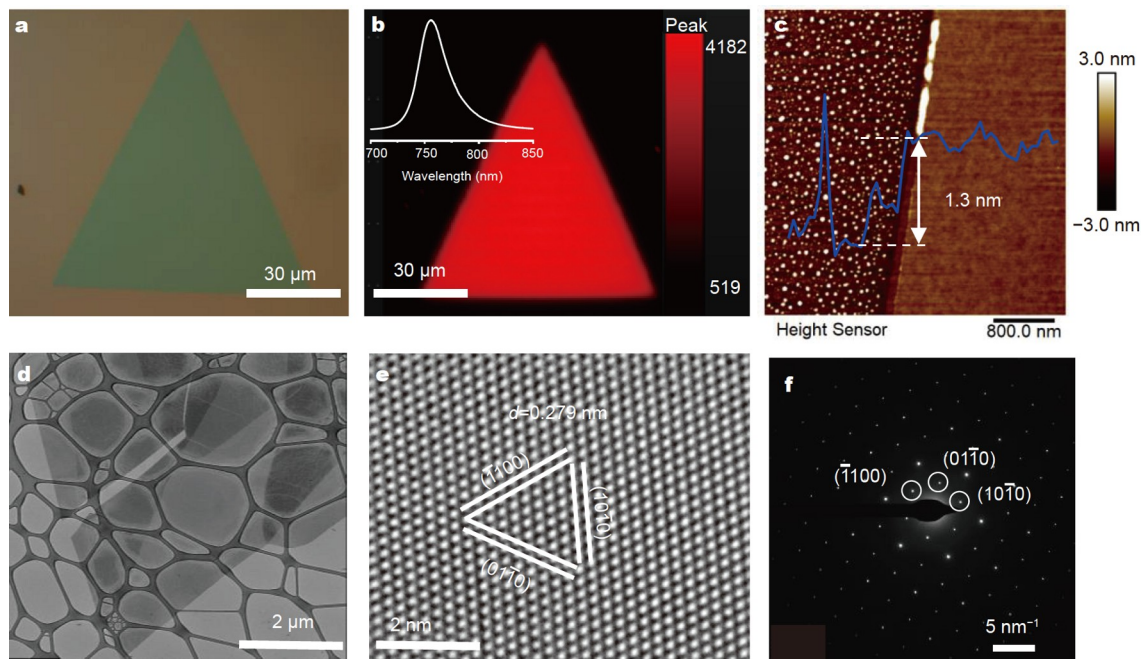
Figure 1 Morphology and structure of the PVD-grown WSe$_2$. (a) Typical optical image of a PVD-grown WSe$_2$ flake. (b) PL mapping at 755 nm of the WSe$_2$ flake. The inset shows the PL spectrum of WSe$_2$, which shows a PL peak at 755 nm. (c) AFM morphological image at the edge of the WSe$_2$ flake. The extracted height profile reveals that the thickness of WSe$_2$ is approximately 1.3 nm. (d) Low-magnification TEM image of a WSe$_2$ flake. (e) HRTEM image and (f) the corresponding Fourier transform pattern of the WSe$_2$ flake.

Next, such high-quality WSe$_2$ flakes were employed to construct mixed-dimensional WS$_2$/WSe$_2$/p-Si unipolar barrier photodetectors. As schematically shown in Fig. 2, the oxide layer on SiO$_2$/p-Si was selectively etched off to expose the p-Si underneath. Then, a PVD-grown WSe$_2$ and mechanically exfoliated WS$_2$ were sequentially transferred to the edge of the p-Si window. Finally, the Ti/Au drain and Ag source electrodes were patterned and deposited.

Then, the structural properties of the unipolar barrier photodetector were explored. Fig. 3a shows an optical image of the device with each component labeled. The Raman spectra of the WS$_2$/WSe$_2$/p-Si heterostructures are shown in Fig. 3b. Typical Raman peaks for WSe$_2$ and WS$_2$ can be observed, and the positions of these peaks are consistent with previously reported values [37,38]. The enlarged Raman features of WSe$_2$ are shown in Fig. S2a, which is consistent with the reported bilayer WSe$_2$ [39]. This phenomenon further confirms its bilayer nature. In addition, the significant quenching of the Raman peaks of WSe$_2$ in WSe$_2$/Si is observed, which could be attributed to the interfacial coupling between the mixed-dimensional heterojunctions [40]. Furthermore, the Raman peaks of WSe$_2$ in WS$_2$/WSe$_2$/Si almost disappeared, which could be due to the thickness of the multilayer WS$_2$ larger than the penetration depth of the excitation laser [38,41,42]. To investigate the dynamics of the photogenerated carriers in the heterostructures, PL measurements were conducted. As shown in Fig. S3, the PL peak of WS$_2$ is significantly quenched after being transferred onto p-Si. This PL quenching is attributed to two reasons. On the one hand, the recombination centers in the interface of WSe$_2$ and p-Si can promote the quenching of PL [11]. On the other hand, the transfer of photogenerated holes from WS$_2$ to p-Si can also bring about the quenching of PL [29]. However, with the insertion of WSe$_2$, the PL peak of WS$_2$ recovered. Because the intercalated WSe$_2$ still allowed the unimpeded transfer of photogenerated holes in 2D WS$_2$ to p-Si, the unfavorable substrate effects were effectively suppressed. In addition, the PL peaks of WSe$_2$ in WS$_2$/WSe$_2$ and WS$_2$/WSe$_2$/p-Si were clearly quenched and redshifted (Fig. 3c), indicating a strong interfacial coupling around WSe$_2$ [43]. Next, the AFM measurement in Fig. 3d illustrates that the thickness of the top WS$_2$ is 84.9 nm. The synchronized KPFM image in Fig. 3e indicates that the Fermi level difference (ΔE_f) between WS$_2$ and WSe$_2$ is 64.1 meV (the calculation process is detailed in Note S1). Moreover, the thickness of the transferred WSe$_2$ is 1.53 nm (Fig. S2b, c), and ΔE_f between WSe$_2$ and p-Si is 101 meV (Fig. 3f).

Afterward, the optoelectronic properties of the WS$_2$/WSe$_2$/p-Si unipolar barrier photodetector were characterized. Fig. 4 displays a schematic diagram of the device together with electrical connections. In this architecture, the resistance of multilayer WS$_2$ is much lower than that of atomically thin WSe$_2$ (Figs S4–S6). Thus, as schematically depicted in Fig. S5, the current enters the WSe$_2$/p-Si heterostructure mainly through WS$_2$. The current-voltage (I-V) curves of the device in the dark and under illumination are presented in Fig. 4b and Fig. S7. An obvious photoresponse was observed, especially in the forward-biased region, revealing the strong photosensitivity of the device. To explore the inner tunneling mechanism, Fowler-Nordheim plots were used. In an optoelectronic device, the direct tunneling (DT) and Fowler-Nordheim tunneling (FNT) effects can be expressed by the following relationships and alternative forms [15,44,45]:

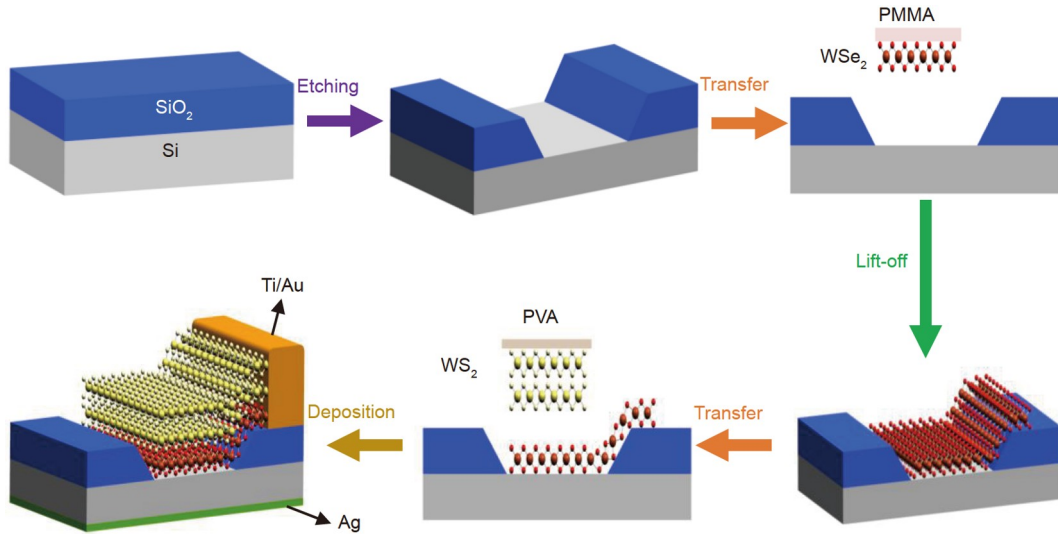$$I_{DT} \propto V \exp\left(-\frac{4\pi d\sqrt{2m*\Phi}}{\hbar}\right),$$

or

Figure 2 Schematic diagram of the fabrication process of the WS₂/WSe₂/p-Si device.
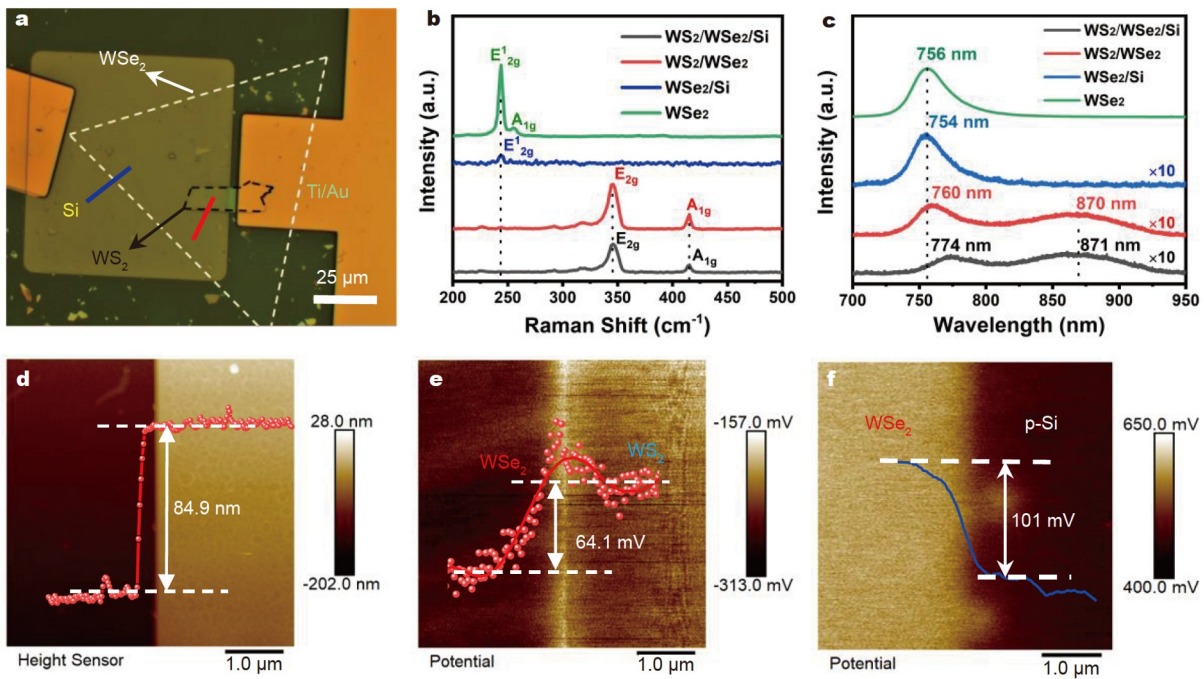

Figure 3 Structural properties of the WS₂/WSe₂/p-Si device. (a) Optical image of the WS₂/WSe₂/p-Si device. The WSe₂ and WS₂ flakes are marked in white and black dashed lines, respectively. The right electrode is the drain, and the metal pad on the left is a marker of the p-Si window. (b) Raman spectra and (c) PL spectra of WSe₂ and WS₂/WSe₂ on SiO₂ and 3D Si substrates. Synchronous measurements for (d) the AFM topography and (e) KPFM images at the red solid line in (a). The thickness of WS₂ is 84.9 nm, and the potential difference between WS₂ and WSe₂ is 64.1 mV. (f) KPFM image at the blue solid line in (a). The potential difference between WSe₂ and p-Si is 101 mV.

$$\ln\left(\frac{I_{DT}}{V^2}\right) \propto \ln\left(\frac{I_{DT}}{V}\right) - \frac{4\pi d\sqrt{2m^*\Phi}}{\hbar}, \tag{1}$$

$$I_{FNT} \propto V^2 \exp\left(-\frac{8\pi d\sqrt{2m^*\Phi^3}}{3\hbar qV}\right),$$

or

$$\ln\left(\frac{I_{FNT}}{V^2}\right) \propto -\frac{8\pi d\sqrt{2m^*\Phi^3}}{3\hbar qV}, \tag{2}$$

where Φ, d, $\hbar$, m^*, and q represent the barrier height, tunneling barrier width, Planck constant ($\sim 1.0545 \times 10^{-34}$ J s), effective mass of the electron, and electronic charge (1.6×10^{-19} C), respectively. According to the above formulas, the DT and FNT can be separated by the different relationships of $\ln(I/V^2)$ and $1/V$. As shown in Fig. 4c, the device exhibits a DT behavior in all forward-biased regions in the dark. Under 405-nm light illumination (Fig. 4d), the device exhibited a DT behavior at a bias voltage (V_{ds}) less than 0.57 V, while it converted to an FNT behavior as the voltage became greater than 0.57 V.

Subsequently, several key performance metrics, including responsivity (R), detectivity (D^*), external quantum efficiency
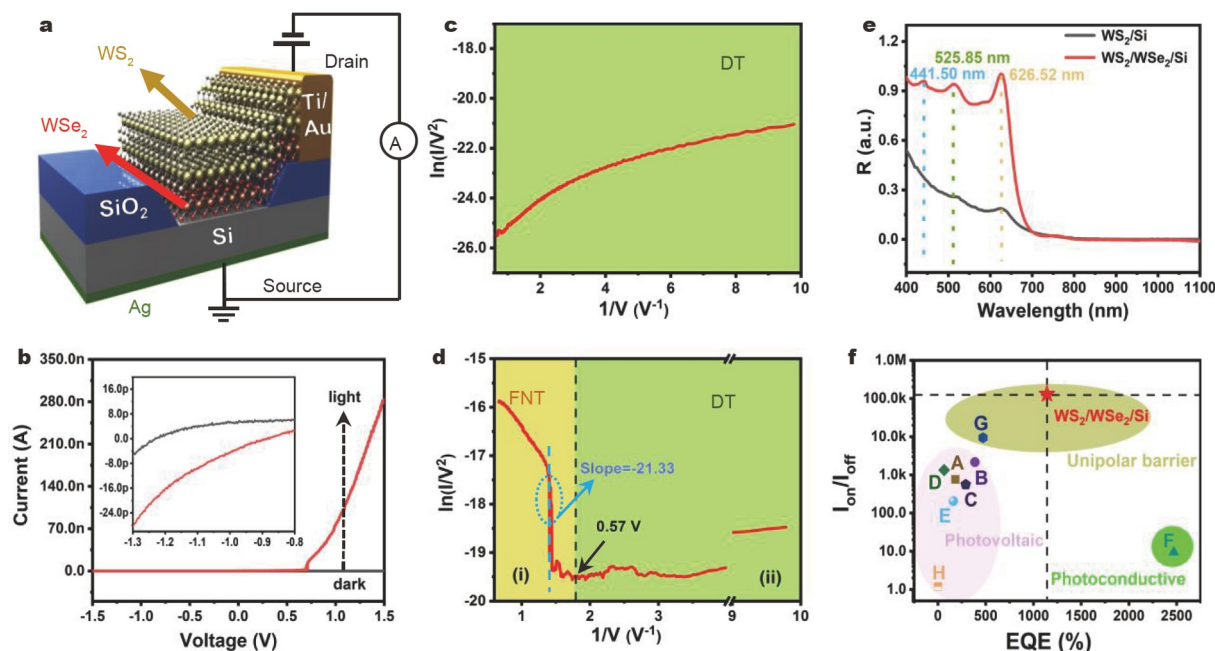
Figure 4 Schematic and characterization of the WS$_2$/WSe$_2$/p-Si unipolar barrier photodetector. (a) Schematic diagram of the device structure together with electrical connections. The top WS$_2$ connects the drain, and the bottom p-Si connects the source. (b) Plots of *I-V* curves under dark and 405-nm light irradiation. Inset is the enlarged *I-V* curves under a negative bias. Fowler-Nordheim plot at the forward drain voltage (c) under dark and (d) 405-nm light illumination. (e) Spectral responsivity of the WS$_2$/p-Si device and WS$_2$/WSe$_2$/p-Si device. (f) Comparison of I_{on}/I_{off} and EQE for different operating mechanism devices. These figures of merit are extracted at V_{ds} = 1.5 V. A, B, C, D, and E represent WS$_2$/p-Si devices with WS$_2$ thicknesses of 14, 35, 55, 78, and 190 nm, respectively. F represents the pure WS$_2$ (79 nm) device. G represents the 73 nm WS$_2$/WSe$_2$/p^{++}-Si device. H represents the WSe$_2$/p-Si device.

(EQE), light on/off ratio (I_{on}/I_{off}), and response time (τ_{rise} and τ_{decay}), were calculated to illustrate the photoelectric properties of the constructed photodetectors (the detailed calculation is available in Note S2). Fig. 4e shows the normalized responsivity of the WS$_2$/p-Si and WSe$_2$/WS$_2$/p-Si devices under different light wavelengths. Both devices exhibit sensitivity in the visible-light regime, and the WSe$_2$/WS$_2$/p-Si device exhibits a high responsivity. As shown in Figs S8 and S9, the counterpart WSe$_2$/p-Si heterostructure exhibits little photosensitivity to visible light, and the Si device also shows low responsivity with a maximum of 965 nm light. Therefore, the photogenerated carriers in the WSe$_2$/WS$_2$/p-Si device are mainly in the top WS$_2$ layer, which is defined as the photon absorber. To compare the differences between the unipolar barrier and conventional p-n heterostructure devices, the optoelectronic properties of the WS$_2$/p-Si devices with different thicknesses of WS$_2$ were measured. As presented in Figs S10–S14, all devices manifest a distinct photoresponse in the forward-biased region, and the device with ~78 nm WS$_2$ (Fig. S13) exhibits the fastest response time and largest potential difference. After inserting atomically thin WSe$_2$ (unipolar barrier device), the EQE and I_{on}/I_{off} of the device significantly increased, far superior to the counterpart photovoltaic effect-based devices, as shown in Fig. 4f. Specifically, at a bias voltage of 1.5 V, I_{on}/I_{off} is higher than 10^5, which outperforms most photoconductive mode-based photodetectors [46–48], and it is even comparable to many state-of-the-art devices based on the photovoltaic effect [29,49–51]. Beyond this, such a design scheme is universally applicable to constructing WS$_2$/WSe$_2$/p^{++}-Si devices, which also exhibit outstanding photodetection capability, including a high I_{on}/I_{off} and fast response speed (G in Fig. 4f and Fig. S15). Although the pure WS$_2$ device operated in the photoconductive mode exhibits a high EQE (F in

Fig. 4f), the low I_{on}/I_{off} and slow response speed (Fig. S6) restrict its further applications. Fig. S16 shows the typical photoswitching characteristics of the device with and without atomically thin WSe$_2$ inserted. Compared with the original WS$_2$/p-Si device, the insertion of WSe$_2$ not only enhances the photoresponse but also significantly suppresses the dark current.

To further understand the photoresponse properties of our WS$_2$/WSe$_2$/p-Si unipolar barrier device, Fig. 5a demonstrates the voltage-dependent photocurrent ($I_{ph} = I_{light} - I_{dark}$) under 405-nm light illumination at 102.69 mW cm^{-2}. A self-driven (V_{ds} = 0 V) photoresponse was observed (Fig. S17), and the photocurrent presented a superlinear dependence on the bias voltage. In photoconductive effect-based devices, high-bias voltages provide strong electric fields to accelerate the separation of photogenerated carriers, featuring a linear increase in the measured photocurrent with the applied bias voltage [35,52]. Clearly, it is not the case for our results. In previous reports, Liao *et al.* [53] and Zhou *et al.* [54] suggested that this superlinear voltage-dependent photocurrent was attributed to the tunneling effect at the metal/semiconductor Schottky junction. Considering the ohmic contacts between the p-Si and Ag electrode [29] and the WS$_2$ flake and Ti/Au electrodes (Fig. S6c) [55], the voltage-driven tunneling effect is not the origin of this phenomenon either. Actually, this superlinear voltage-dependent photocurrent can be attributed to the voltage-driven carrier multiplication and tunneling effects (the detailed process is described in the DISCUSSION section). Similar to previous reports [56–58], we assume that the shot noise from the dark current dominates the total noise, and R and D* of the WS$_2$/WSe$_2$/p-Si device under different bias voltages are calculated in Fig. 5b. Voltage-dependent superlinear R and D* were observed, and the best figures of merit were obtained at a bias voltage of 1.5 V. Fig. 5c shows
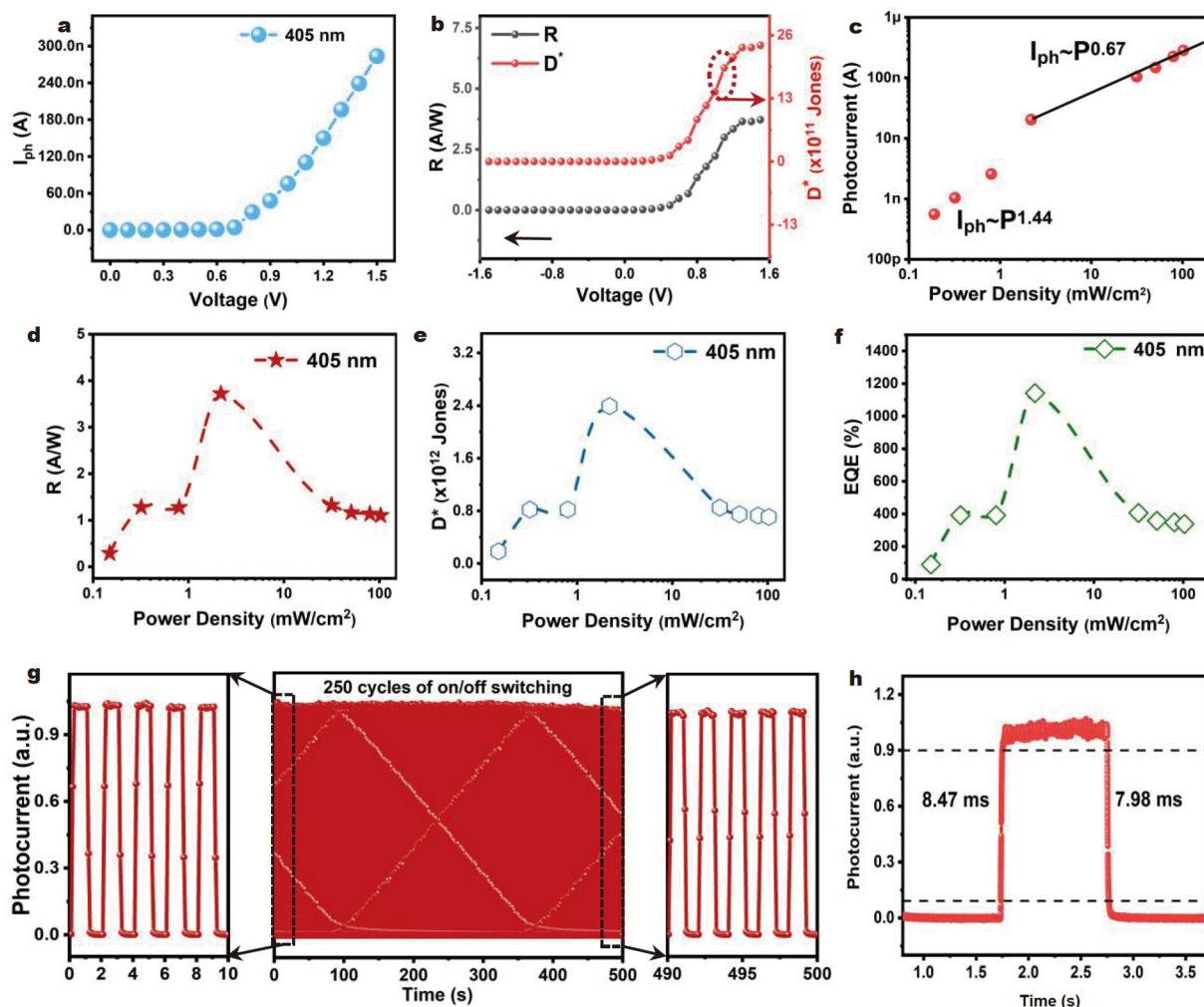
Figure 5 Optoelectronic characteristics of the WS$_2$/WSe$_2$/p-Si unipolar barrier photodetector. (a) Photocurrent of the WS$_2$/WSe$_2$/p-Si device along with the bias voltage. (b) Bias voltage-dependent R and D^* of the WS$_2$/WSe$_2$/p-Si device. (c) Power-dependent photocurrent at V_{ds} = 1.5 V. (d–f) Calculated R, D^*, and EQE with different light intensities at V_{ds} = 1.5 V. (g) Photoswitching characteristics of the device under pulse light. (h) Response time of the device at V_{ds} = 1.5 V. The corresponding τ_{rise} and τ_{decay} are 8.47 and 7.98 ms, respectively.

photocurrents extracted under different incident intensities at a bias voltage of 1.5 V. The photocurrent increased as the light intensity increased, and it followed the equation $I_{ph} \propto P^{1.44}$ for weak light and $I_{ph} \propto P^{0.67}$ for strong light. This inhomogeneity of the power exponent originates from the chemical adsorbates on the WS$_2$ surface (the details are described in Note S3). Power-dependent R, D^*, and EQE are shown in Fig. 5d–f, respectively. Shoulder peaks were observed, which can be attributed to the different light intensity dependences of the photocurrents (the details are described in Note S3). Remarkably, our device achieved a high R of 3.72 A W^{-1}, along with a high D^* of 2.39 × 10^{12} Jones and a high EQE of 1140% at a light intensity of 2.19 mW cm^{-2}. In addition, based on the measured noise spectral density (S_{noise}) in Fig. S18, the highest D^* was calculated to be 2.1 × 10^{11} Jones.

Then, the stability and response speed of the unipolar barrier device were also investigated. Fig. 5g shows the normalized time-dependent photocurrent curve under a periodic 405-nm light stimulation. Our device exhibited definite switching characteristics, and the photocurrent remained nearly unchanged after 250 operation cycles, suggesting the high durability of the

photodetector. To evaluate the response time, the dynamic photocurrent signal of the unipolar barrier device was recorded through an oscilloscope. As presented in Fig. 5h, the rise time (τ_{rise}) and decay time (τ_{decay}) were calculated to be 8.47 and 7.98 ms, respectively, which are slightly faster than those of the original WS$_2$/p-Si device (τ_{rise}/τ_{decay} = 15.09/8.68 ms). This response speed is not prominent, which is affected by the thick p-Si. It can be further accelerated by reducing the thickness of p-Si. For an explicit comparison, Table 1 summarizes the key parameters of our WS$_2$/WSe$_2$/p-Si photodetector and other WS$_2$-based devices. The photoresponse of our device at 405 nm reflected a typical photoresponse level (Fig. 4e), and the parameters of other devices were extracted from the wavelength with the highest photoresponse. The typical photoresponse of our unipolar barrier device is at the top level compared with the highest photoresponse of other WS$_2$-based devices, revealing the superiority of our unipolar barrier structure for photodetection applications.

DISCUSSION
Sequentially, the working mechanism for the outstanding pho-

Table 1 Key parameters of the WS$_2$/WSe$_2$/p-Si device and other WS$_2$-based devices[a]

| Devices	Bias (V)	R (A W^{-1})	EQE (%)	D^* (Jones)	I_{on}/I_{off}	Response/recovery time	λ (nm)	Ref.
WS$_2$/WSe$_2$/Si	1.5	3.72	1140	2.39×10^{12}	>10^5	8.47/7.98 ms	405	This work
WS$_2$	30	9.2×10^{-5}	~0.025	N/A	N/A	5.3/5.3 ms	458	[37]
WS$_2$	20	0.0188	~4.39	N/A	<10	60/190 ms	532	[36]
WS$_2$	9	0.70	137	2.7×10^9	N/A	9.8/8.7 s	635	[59]
WS$_2$	1	3.07	763	N/A	<6	0.37/5.02 s	500	[60]
Gr/WS$_2$/Gr	5	3.50	933	1.6×10^{10}	N/A	N/A	532	[61]
WS$_2$/PbS QDs	1.5	14	~2150	3.9×10^8	<10	153/226 μs	808	[62]
WS$_2$/MoS$_2$	0	4.36×10^{-3}	~1.02	4.4×10^{13}	10^2	4/4 ms	532	[63]
WS$_2$/Ge	0	0.6345	50.8	4.3×10^{11}	~10^5	42.9/29.6 μs	1550	[64]
WS$_2$/Si	−2	1.10	~216	5×10^{11}	N/A	42/76 ms	631	[65]
WS$_2$/Si	−5	5.70	~1090	N/A	10^2	670/998 μs	660	[66]
Bi/WS$_2$/Si	2	0.42	~82.2	1.36×10^{13}	10^6	100/100 ms	635	[67]

a) Ref: reference; Gr: graphene; N/A: no data.
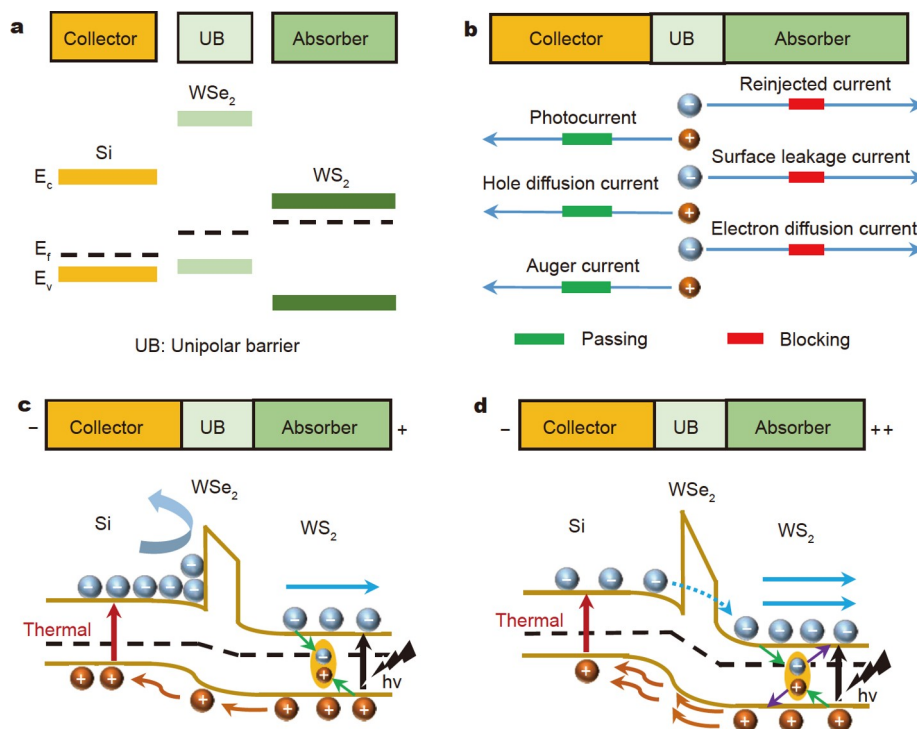
Figure 6 Dark current and photocurrent mechanisms of the WS$_2$/WSe$_2$/p-Si unipolar barrier photodetector. (a) Energy band arrangement of the WS$_2$/WSe$_2$/p-Si heterojunction before contact. E_c, E_f, and E_v are the conduction band minimum, Fermi level, and valence band maximum, respectively. (b) Dark current components in this unipolar barrier photodetector. (c) Energy band arrangement of the WS$_2$/WSe$_2$/p-Si unipolar barrier photodetector under a small-bias condition. A large conduction band barrier is demonstrated, in which electrons in the conduction band are impeded by the barrier, while the photoexcited holes' flow is unimpeded. (d) Energy band arrangement of the WS$_2$/WSe$_2$/p-Si device under a high-bias condition. The flow of photogenerated electrons and holes is accelerated, and thermal electrons on the conduction band of the p-Si tunnel move into WS$_2$.

todetection performance of our unipolar barrier device was qualitatively elucidated. Based on the above KPFM analysis and relevant reports [67–69], the band alignments of the WS$_2$/WSe$_2$/p-Si heterostructure were established before contact. As shown in Fig. 6a, the large bandgap of the atomically thin WSe$_2$ brings about a high-conduction band barrier and zero valence band offset from the surrounding p-Si and WS$_2$. Here, the inserted WSe$_2$ plays a critical role in device operation. First, in a traditional WS$_2$/p-Si p-n heterostructure photodetector, the traps in

the depletion region contribute numerous dark current sources, resulting in a considerable reverse current (Fig. S19) [7]. For the WS$_2$/WSe$_2$/p-Si structure, several dark current components, such as electron diffusion current, reinjected current, and surface leakage current, were blocked by the high barrier and the absence of depletion regions (the schematic process is illustrated in Fig. 6b and Fig. S20). Moreover, the DT behavior contributes to the low dark current. Accordingly, such a unipolar barrier structure was designed to suppress the dark current. Second,

several electron-hole pairs were generated in the WS_2 layer under light illumination (as marked by the black arrow in Fig. 6c). Subsequently, driven by the applied forward-bias voltage, these photogenerated carriers were separated in opposite directions (as marked by the blue and brown arrows in Fig. 6c). During this process, some electron-hole pairs were bounded by the emerging exciton binding and defect traps (as marked by the green arrows in Fig. 6c). Under a small-bias condition, these bounded carriers were hardly ionized and eventually recombined, which cannot contribute to the photocurrent. The other photogenerated electrons were quickly extracted by the drain electrode, and holes flowed unimpeded to the p-Si across a nearly-zero valence band offset. In principle, the photogenerated holes collected in p-Si are majority carriers with a low probability of recombining with electrons (minority carrier), enabling a high photocurrent (Figs S21 and S22). When a high forward bias voltage was applied, the velocity of the photogenerated carriers was very fast. These energetic carriers strongly impinged on bounded carriers, causing their continuous ionization (purple arrows in Fig. 6d). Thus, the number of photogenerated carriers was multiplied, greatly enhancing the photocurrent [70]. Fig. S23 shows the voltage-dependent I_{on}/I_{off} of the unipolar barrier device. Obviously, I_{on}/I_{off} sharply increased with the increase in the bias voltage, further demonstrating that the superlinear photocurrent is driven by the carrier multiplication effect [70]. Furthermore, under illumination, the Fowler-Nordheim curve in Fig. 4d illustrates that the device operating behavior changed from DT to FNT when the bias voltage was greater than 0.57 V. Therefore, the thermal electrons in the p-Si (as marked by the red arrow in Fig. 6d) can tunnel to WS_2 through the FNT under a high-bias condition (as marked by the blue dashed arrow in Fig. 6d), bringing about additional photocurrents. Such voltage-driven carrier multiplication and electron tunneling effects result in the superlinear voltage-dependent photocurrent in Fig. 5a. In addition, the photoresponse speed depends on the photogenerated carrier transport rate, which is severely influenced by the collision of carriers with interfacial defect states [71]. In the WS_2/WSe_2/p-Si unipolar barrier device, the unfavorable substrate effect around WS_2 was effectively suppressed, which promotes the migration of photogenerated carriers and improves the photoresponse speed. Then, the photodetection performance of this unipolar device is inferior to the reported all-2D device [7], which can be attributed to the adoption of a thick p-Si. The thick p-Si extends the moving distance of photogenerated holes, leading to the consumption of the collected holes. However, this 2D/3D mixed-dimensional device brings about many advantages. On the one hand, the combination of novel 2D materials with mature Si technology lays the foundation for the practical application of the device in the future. On the other hand, different from previous reports using nBn or pBp heterojunctions [7,19,21,22,28], we propose an nBp structure to construct the unipolar barrier photodetector. This structure not only broadens the family of unipolar barrier photodetectors but also provides inspiration for building other high-performance optoelectronic devices. To further improve the device performance, experimental explorations face further challenges, such as using an optimized p-Si layer to passivate its internal defect states.

Third, a large number of defect states exist on the surface of p-Si, which act as recombination centers for photogenerated carriers, resulting in severe recombination losses. In our WS_2/WSe_2/ p-Si device, the intercalated WSe_2 separates WS_2 from p-Si, which mitigates the detrimental substrate effects [72]. This condition is beneficial to reducing the recombination loss of photogenerated carriers and enhancing the photoresponse speed (Fig. 5h). Meanwhile, WSe_2 underneath WS_2 preserves the intrinsic optoelectronic properties in WS_2, which corresponds to the recovered PL peak in Fig. S3. In addition, the atomically thin WSe_2 enables the interaction of the carrier wave function in WS_2 and p-Si, enabling the quantum tunneling of carriers through the WSe_2 layer [72]. Therefore, the alliance of the above favorable factors brings about the outstanding photodetection capabilities of our WS_2/WSe_2/p-Si unipolar barrier photodetector.

CONCLUSIONS

In summary, we constructed a mixed-dimensional WS_2/WSe_2/p-Si unipolar barrier photodetector *via* sequentially transferring PVD-grown WSe_2 and mechanically exfoliated WS_2 onto the p-Si window. In this device, 2D WS_2 acts as the photon absorber, atomically thin WSe_2 as the unipolar barrier, and 3D p-Si as the photogenerated carrier collector. This unipolar barrier structure has many advantages. On the one hand, it can filter out several dark current components without suppressing the photocurrent. On the other hand, the insertion of WSe_2 effectively mitigates the adverse substrate effects and allows the top WS_2 to preserve its intrinsic optoelectronic properties. Benefiting from these favorable factors, the photodetection performance metrics of our WS_2/WSe_2/p-Si device have been significantly improved compared with the conventional WS_2/p-Si device, shedding light on advancing the revolutionary design of 2D material-based optoelectronic devices.

1 Lopez-Sanchez O, Lembke D, Kayci M, *et al*. Ultrasensitive photodetectors based on monolayer MoS_2. Nat Nanotech, 2013, 8: 497–501

2 Bernardi M, Palummo M, Grossman JC. Extraordinary sunlight absorption and one nanometer thick photovoltaics using two-dimensional monolayer materials. Nano Lett, 2013, 13: 3664–3670

3 He Z, Sheng Y, Rong Y, *et al*. Layer-dependent modulation of tungsten disulfide photoluminescence by lateral electric fields. ACS Nano, 2015, 9: 2740–2748

4 Wang QH, Kalantar-Zadeh K, Kis A, *et al*. Electronics and optoelectronics of two-dimensional transition metal dichalcogenides. Nat Nanotech, 2012, 7: 699–712

5 Liu Y, Weiss NO, Duan X, *et al*. Van der Waals heterostructures and devices. Nat Rev Mater, 2016, 1: 16042

6 Miao J, Liu X, Jo K, *et al*. Gate-tunable semiconductor heterojunctions from 2D/3D van der Waals interfaces. Nano Lett, 2020, 20: 2907–2915

7 Chen Y, Wang Y, Wang Z, *et al*. Unipolar barrier photodetectors based on van der Waals heterostructures. Nat Electron, 2021, 4: 357–363

8 Konstantatos G, Badioli M, Gaudreau L, *et al*. Hybrid graphene-quantum dot phototransistors with ultrahigh gain. Nat Nanotech, 2012, 7: 363–368

9 Massicotte M, Schmidt P, Vialla F, *et al*. Picosecond photoresponse in van der Waals heterostructures. Nat Nanotech, 2016, 11: 42–46

10 Georgiou T, Jalil R, Belle BD, *et al*. Vertical field-effect transistor based on graphene-WS_2 heterostructures for flexible and transparent electronics. Nat Nanotech, 2013, 8: 100–103

11 Luo P, Wang F, Qu J, *et al*. Self-driven WSe_2/Bi_2O_2Se van der Waals heterostructure photodetectors with high light on/off ratio and fast response. Adv Funct Mater, 2021, 31: 2008351

12 Lee JB, Lim YR, Katiyar AK, *et al*. Direct synthesis of a self-assembled WSe_2/MoS_2 heterostructure array and its optoelectrical properties. Adv Mater, 2019, 31: 1904194

13 Lu J, Yan J, Yao J, *et al.* All-dielectric nanostructure Fabry-Pérot-Enhanced mie resonances coupled with photogain modulation toward ultrasensitive In$_2$S$_3$ photodetector. Adv Funct Mater, 2021, 31: 2007987

14 Koppens FHL, Mueller T, Avouris P, *et al.* Photodetectors based on graphene, other two-dimensional materials and hybrid systems. Nat Nanotech, 2014, 9: 780–793

15 Gao F, Chen H, Feng W, *et al.* High-performance van der Waals metal-insulator-semiconductor photodetector optimized with valence band matching. Adv Funct Mater, 2021, 31: 2104359

16 Wu F, Li Q, Wang P, *et al.* High efficiency and fast van der Waals hetero-photodiodes with a unilateral depletion region. Nat Commun, 2019, 10: 4663

17 Huo N, Gupta S, Konstantatos G. MoS$_2$-HgTe quantum dot hybrid photodetectors beyond 2 μm. Adv Mater, 2017, 29: 1606576

18 Kopytko M, Rogalski A. HgCdTe barrier infrared detectors. Prog Quantum Electron, 2016, 47: 1–18

19 Maimon S, Wicks GW. *nBn* detector, an infrared detector with reduced dark current and higher operating temperature. Appl Phys Lett, 2006, 89: 151109

20 Martyniuk P, Kopytko M, Rogalski A. Barrier infrared detectors. Opto-Electron Rev, 2014, 22: 127–146

21 Kim HS, Cellek OO, Lin ZY, *et al.* Long-wave infrared *nBn* photodetectors based on InAs/InAsSb type-II superlattices. Appl Phys Lett, 2012, 101: 161114

22 Kim HS, Plis E, Rodriguez JB, *et al.* Mid-IR focal plane array based on type-II InAs/GaSb strain layer superlattice detector with *nBn* design. Appl Phys Lett, 2008, 92: 183502

23 Wu D, Guo J, Du J, *et al.* Highly polarization-sensitive, broadband, self-powered photodetector based on graphene/PdSe$_2$/germanium heterojunction. ACS Nano, 2019, 13: 9907–9917

24 Zeng L, Han W, Wu SE, *et al.* Graphene/PtSe$_2$/pyramid Si van der Waals Schottky junction for room-temperature broadband infrared light detection. IEEE Trans Electron Devices, 2022, 69: 6212–6216

25 Wu D, Guo C, Wang Z, *et al.* A defect-induced broadband photodetector based on WS$_2$/pyramid Si 2D/3D mixed-dimensional heterojunction with a light confinement effect. Nanoscale, 2021, 13: 13550–13557

26 Wu D, Xu M, Zeng L, *et al.* *In situ* fabrication of PdSe$_2$/GaN Schottky junction for polarization-sensitive ultraviolet photodetection with high dichroic ratio. ACS Nano, 2022, 16: 5545–5555

27 Wu D, Jia C, Shi F, *et al.* Mixed-dimensional PdSe$_2$/SiNWA heterostructure based photovoltaic detectors for self-driven, broadband photodetection, infrared imaging and humidity sensing. J Mater Chem A, 2020, 8: 3632–3642

28 Rodriguez JB, Plis E, Bishop G, *et al.* *nBn* structure based on InAs/GaSb type-II strained layer superlattices. Appl Phys Lett, 2007, 91: 043514

29 Gao W, Zheng Z, Huang L, *et al.* Self-powered SnS$_{1-x}$Se$_x$ alloy/silicon heterojunction photodetectors with high sensitivity in a wide spectral range. ACS Appl Mater Interfaces, 2019, 11: 40222–40231

30 Zhang Z, Chen P, Duan X, *et al.* Robust epitaxial growth of two-dimensional heterostructures, multiheterostructures, and superlattices. Science, 2017, 357: 788–792

31 Li H, Wu J, Huang X, *et al.* Rapid and reliable thickness identification of two-dimensional nanosheets using optical microscopy. ACS Nano, 2013, 7: 10344–10353

32 Addou R, Wallace RM. Surface analysis of WSe$_2$ crystals: Spatial and electronic variability. ACS Appl Mater Interfaces, 2016, 8: 26400–26406

33 Chen YZ, Medina H, Su TY, *et al.* Ultrafast and low temperature synthesis of highly crystalline and patternable few-layers tungsten diselenide by laser irradiation assisted selenization process. ACS Nano, 2015, 9: 4346–4353

34 Zheng Z, Zhang T, Yao J, *et al.* Flexible, transparent and ultra-broadband photodetector based on large-area WSe$_2$ film for wearable devices. Nanotechnology, 2016, 27: 225501

35 Island JO, Blanter SI, Buscema M, *et al.* Gate controlled photocurrent generation mechanisms in high-gain In$_2$Se$_3$ phototransistors. Nano Lett, 2015, 15: 7853–7858

36 Lan C, Li C, Yin Y, *et al.* Large-area synthesis of monolayer WS$_2$ and its ambient-sensitive photo-detecting performance. Nanoscale, 2015, 7: 5974–5980

37 Perea-López N, Elías AL, Berkdemir A, *et al.* Photosensor device based on few-layered WS$_2$ films. Adv Funct Mater, 2013, 23: 5511–5517

38 Zhou X, Hu X, Zhou S, *et al.* Tunneling diode based on WSe$_2$/SnS$_2$ heterostructure incorporating high detectivity and responsivity. Adv Mater, 2018, 30: 1703286

39 del Corro E, Terrones H, Elias A, *et al.* Excited excitonic states in 1L, 2L, 3L, and bulk WSe$_2$ observed by resonant raman spectroscopy. ACS Nano, 2014, 8: 9629–9635

40 Kim HS, Patel M, Kim J, *et al.* Growth of wafer-scale standing layers of WS$_2$ for self-biased high-speed UV-visible-NIR optoelectronic devices. ACS Appl Mater Interfaces, 2018, 10: 3964–3974

41 Wu F, Xia H, Sun H, *et al.* AsP/InSe van der Waals tunneling heterojunctions with ultrahigh reverse rectification ratio and high photosensitivity. Adv Funct Mater, 2019, 29: 1900314

42 Yang S, Liu K, Han W, *et al.* Salt-assisted growth of p-type Cu$_9$S$_5$ nanoflakes for p-n heterojunction photodetectors with high responsivity. Adv Funct Mater, 2020, 30: 1908382

43 Tongay S, Fan W, Kang J, *et al.* Tuning interlayer coupling in large-area heterostructures with CVD-grown MoS$_2$ and WS$_2$ monolayers. Nano Lett, 2014, 14: 3185–3190

44 Lei T, Lv W, Lv W, *et al.* High detectivity and responsivity in black phosphorus/SnS$_2$ heterostructure with broken-gap energy band alignment. Jpn J Appl Phys, 2021, 60: 065003

45 Tao L, Yao B, Yue Q, *et al.* Vertically stacked Bi$_2$Se$_3$/MoTe$_2$ heterostructure with large band offsets for nanoelectronics. Nanoscale, 2021, 13: 15403–15414

46 Chang C, Chen W, Chen Y, *et al.* Recent progress on two-dimensional materials. Acta Physico Chim Sin, 2021, 37: 2108017

47 Huo N, Konstantatos G. Recent progress and future prospects of 2D-based photodetectors. Adv Mater, 2018, 30: 1801164

48 Guan X, Yu X, Periyanagounder D, *et al.* Recent progress in short- to long-wave infrared photodetection using 2D materials and heterostructures. Adv Opt Mater, 2021, 9: 2001708

49 Ahmad W, Liu J, Jiang J, *et al.* Strong interlayer transition in few-layer InSe/PdSe$_2$ van der Waals heterostructure for near-infrared photodetection. Adv Funct Mater, 2021, 31: 2104143

50 Jang H, Seok Y, Choi YT, *et al.* High-performance near-infrared photodetectors based on surface-doped InSe. Adv Funct Mater, 2021, 31: 2006788

51 Sun J, Wang Y, Guo S, *et al.* Lateral 2D WSe$_2$ p-n homojunction formed by efficient charge-carrier-type modulation for high-performance optoelectronics. Adv Mater, 2020, 32: 1906499

52 Zheng ZQ, Yao JD, Yang GW. Growth of centimeter-scale high-quality In$_2$Se$_3$ films for transparent, flexible and high performance photodetectors. J Mater Chem C, 2016, 4: 8094–8103

53 Liao M, Wang X, Teraji T, *et al.* Light intensity dependence of photocurrent gain in single-crystal diamond detectors. Phys Rev B, 2010, 81: 033304

54 Zhou Y, Wang L, Wang J, *et al.* Highly sensitive, air-stable photodetectors based on single organic sub-micrometer ribbons self-assembled through solution processing. Adv Mater, 2008, 20: 3745–3749

55 Zhou Y, Zhang L, Gao W, *et al.* A reasonably designed 2D WS$_2$ and CdS microwire heterojunction for high performance photoresponse. Nanoscale, 2021, 13: 5660–5669

56 Zhou X, Gan L, Tian W, *et al.* Ultrathin SnSe$_2$ flakes grown by chemical vapor deposition for high-performance photodetectors. Adv Mater, 2015, 27: 8035–8041

57 Luo Z, Yang M, Wu D, *et al.* Rational design of WSe$_2$/WS$_2$/WSe$_2$ dual junction phototransistor incorporating high responsivity and detectivity. Small Methods, 2022, 6: 2200583

58 Yang M, Luo Z, Gao W, *et al.* Robust deposition of sub-millimeter WSe$_2$ drive ultrasensitive gate-tunable 2D material photodetectors. Adv Opt Mater, 2022, 10: 2200717

59 Yao JD, Zheng ZQ, Shao JM, *et al.* Stable, highly-responsive and broadband photodetection based on large-area multilayered WS$_2$ films grown by pulsed-laser deposition. Nanoscale, 2015, 7: 14974–14981

60 Chen Y, Gan L, Li H, *et al.* Achieving uniform monolayer transition

metal dichalcogenides film on silicon wafer *via* silanization treatment: A typical study on WS$_2$. Adv Mater, 2017, 29: 1603550

61 Tan H, Fan Y, Zhou Y, *et al.* Ultrathin 2D photodetectors utilizing chemical vapor deposition grown WS$_2$ with graphene electrodes. ACS Nano, 2016, 10: 7866–7873

62 Yu Y, Zhang Y, Song X, *et al.* PbS-decorated WS$_2$ phototransistors with fast response. ACS Photonics, 2017, 4: 950–956

63 Wu W, Zhang Q, Zhou X, *et al.* Self-powered photovoltaic photodetector established on lateral monolayer MoS$_2$-WS$_2$ heterostructures. Nano Energy, 2018, 51: 45–53

64 Wu D, Guo J, Wang C, *et al.* Ultrabroadband and high-detectivity photodetector based on WS$_2$/Ge heterojunction through defect engineering and interface passivation. ACS Nano, 2021, 15: 10119–10129

65 Chowdhury RK, Maiti R, Ghorai A, *et al.* Novel silicon compatible p-WS$_2$ 2D/3D heterojunction devices exhibiting broadband photoresponse and superior detectivity. Nanoscale, 2016, 8: 13429–13436

66 Lan C, Li C, Wang S, *et al.* Zener tunneling and photoresponse of a WS$_2$/Si van der Waals heterojunction. ACS Appl Mater Interfaces, 2016, 8: 18375–18382

67 Yao J, Zheng Z, Shao J, *et al.* Promoting photosensitivity and detectivity of the Bi/Si heterojunction photodetector by inserting a WS$_2$ layer. ACS Appl Mater Interfaces, 2015, 7: 26701–26708

68 Kang J, Tongay S, Zhou J, *et al.* Band offsets and heterostructures of two-dimensional semiconductors. Appl Phys Lett, 2013, 102: 012111

69 Zheng Z, Yao J, Wang B, *et al.* Self-assembly high-performance UV-vis-NIR broadband β-In$_2$Se$_3$/Si photodetector array for weak signal detection. ACS Appl Mater Interfaces, 2017, 9: 43830–43837

70 Yao J, Deng Z, Zheng Z, *et al.* Stable, fast UV-vis-NIR photodetector with excellent responsivity, detectivity, and sensitivity based on α-In$_2$Te$_3$ films with a direct bandgap. ACS Appl Mater Interfaces, 2016, 8: 20872–20879

71 Zhu X, Lin F, Zhang Z, *et al.* Enhancing performance of a GaAs/AlGaAs/GaAs nanowire photodetector based on the two-dimensional electron-hole tube structure. Nano Lett, 2020, 20: 2654–2659

72 Tao L, Chen Z, Li X, *et al.* Hybrid graphene tunneling photoconductor with interface engineering towards fast photoresponse and high responsivity. npj 2D Mater Appl, 2017, 1: 32

Author contributions   Chen Y, Du C and Zheng Z supervised the project and the experiment. Huang Z performed the main experiments and wrote this paper. Yang M and Qiu Z conceived the idea and completed the rest of the experiment. The other authors helped analyze the result, contributed to the theoretical analysis and helped write this paper. All authors contributed to the general discussion.

Conflict of interest   The authors declare that they have no conflict of interest.

Supplementary information   Experimental details and supporting data are available in the online version of the paper.
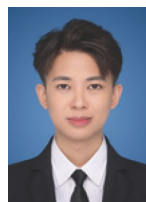
Zihao Huang is a Master candidate at the School of Materials and Energy, Guangdong University of Technology. He received his BSc degree from Dongguan University of Technology in 2020. His current research focuses on designing intelligent 2D material devices for photodetection applications.

Yu Chen received her BSc degree from Wuhan Institute of Technology in 2015 and her Master's degree from Sun Yat-sen University in 2017. Later, she joined the Analysis and Test Center of Guangdong University of Technology and now is responsible for AFM testing. Her research interests are the properties and synthesis of 2D materials and the application expansion of AFM.

Chun Du is a lecturer at the Institute of Photonics Technology, Jinan University. She received her PhD degree in materials physics and chemistry from the School of Materials Science and Engineering, Sun Yat-sen University, in 2020. Her research interests mainly focus on the synthesis of 2D materials and the investigation of their applications in the field of photocatalysis and photodetector.

Zhaoqiang Zheng received his BSc degree from Hunan University in 2011 and his PhD degree from Sun Yat-sen University in 2017. Then, he joined the School of Materials and Energy, Guangdong University of Technology, and currently is an associate professor. His research interests are the design, synthesis, and photodetection applications of novel 2D materials and their heterostructures.

混合维度WS$_2$/WSe$_2$/Si单极势垒异质结构用于高性能光电探测

黄梓豪[1]，杨孟孟[1]，邱智聪[1]，罗中通[1]，陈瑜[2*]，杜纯[3*]，姚健东[4]，董华峰[5]，郑照强[1*]，李京波[6]

摘要   单极势垒异质结构可以选择性地降低暗电流，但不影响光电流，是一种构建高性能光电探测器的有效策略. 特别地，具有可调谐能带结构和自钝化表面的二维(2D)材料不仅能满足能带匹配要求，而且避免了界面缺陷和晶格失配，有助于设计单极势垒异质结构. 这里，我们展示了一种混合维度WS$_2$/WSe$_2$/p-Si单极势垒异质结光电探测器. 其中，2D WS$_2$充当光子吸收体，原子级厚度的WSe$_2$充当单极势垒，3D p-Si充当光生载流子收集器. 插入的WSe$_2$不仅减轻了有害的衬底效应，而且形成了高导带势垒，可以过滤掉若干暗电流分量，同时不影响光电流. 在隧穿效应和载流子倍增效应的驱动下，该WS$_2$/WSe$_2$/p-Si器件表现出高于10^{5}的高开/关比、2.39 × 10^{12} Jones的高探测度和8.47/7.98毫秒的快速上升/衰减时间. 这些优点显著优于传统的WS$_2$/p-Si器件，为设计高性能的光电器件开辟了一个新方案.